Materials Today Communications 42 (2025) 111177

Contents lists available at ScienceDirect

Materials Today Communications

journal homepage: www.elsevier.com/locate/mtcomm

Machine learning based insights for metal-organic frameworks synthesis: A comparative and explainable analysis of ZIF-8 morphology

Yuncheng Du [a,*], Cristina Sanchez [a], Dongping Du [b]

[a] Department of Biomedical Engineering, University of Houston, Houston, TX, USA
[b] Department of Industrial, Manufacturing and Systems Engineering, Texas Tech University, Lubbock, TX, USA

ARTICLE INFO

Keywords:
Machine learning
Porous nanomaterials
ZIF-8
Synthesis optimization
Explainable AI
Neural network

ABSTRACT

Metal-organic frameworks (MOFs) such as zeolitic imidazolate framework-8 (ZIF-8) are promising nanomaterials for various applications like drug delivery and energy storage. The efficacy of ZIF-8 in these applications highly depends on its morphology, including size and shape. However, understanding and controlling morphology during synthesis is challenging due to the complex interactions among synthesis conditions such as precursor concentration and reaction temperature. Traditional trial-and-error methods for morphology optimization are inefficient and cannot effectively account for the combined effects of conditions. Machine learning (ML) offers a powerful alternative for morphology prediction, which can accelerate the reverse engineering process to better understand how synthesis conditions affect morphology. Despite recent advances, developing accurate ML models and selecting the appropriate ones for specific applications remain a challenge. This study addresses these issues by experimentally investigating how variations in synthesis conditions, such as precursor concentrations, solvent properties, and temperature, affect ZIF-8 morphology. Using experimental data, this work further built and compared three ML models: Random Forest (RF), Support Vector Regressor (SVR), and Neural Network (NN). Among these, the NN model has the best performance in terms of R-squared and mean squared errors. These ML models provide insights into how synthesis conditions affect ZIF-8, thus setting the basis for future studies aimed at optimizing conditions and guiding more efficient manufacturing strategy to expand the applications of this versatile nanomaterial.

1. Introduction

Metal-organic frameworks (MOFs) are a school of nanomaterials made from metal ions and organic ligands, which have porous structures with high surface areas and tunable properties [1]. Among these different MOFs, zeolitic imidazolate framework-8 (ZIF-8) has recently gained growing attention. ZIF-8 is made from zinc ions and imidazolate ligands, which creates a robust and highly porous network suitable for applications such as drug delivery and water purification. For example, the tunable size and surface area of ZIF-8 not only facilitates efficient loading of therapeutic agents for targeted drug delivery but also enables effective adsorption of contaminants in water purification.

Despite its potential, the performance of ZIF-8 in these applications critically depends on its morphology, including size and shape. However, achieving precise control over these morphological properties during synthesis is challenging due to the complex relationships of synthesis conditions, such as the concentration of raw materials and reaction temperature. To overcome the challenge, it is critical to understand how different synthesis conditions affect the resulting morphology of ZIF-8 and develop strategies for controlling these conditions with high precision for future large-scale material manufacturing [2].

Current approaches for understanding ZIF-8 synthesis and controlling its morphology generally rely on trial-and-error methods, which are generally inefficient and time-consuming. Computational models, such as those using machine learning (ML) algorithms, offer a powerful alternative, which offer valuable insights for ZIF-8 synthesis and reduce experimental costs by predicting the outcomes of future experiments based on historical data [3]. Recent advances in ML have demonstrated their potential to predict ZIF-8 nucleation and growth [4]. However, existing models focus on individual synthesis conditions at a time, which limits their ability to address the multifactorial nature of ZIF-8 synthesis. This limitation also hinders a deep understanding of how synthesis conditions collectively affect ZIF-8 morphology.

---

* Corresponding author.
E-mail address: ydu20@uh.edu (Y. Du).

https://doi.org/10.1016/j.mtcomm.2024.111177
Received 26 September 2024; Received in revised form 26 November 2024; Accepted 30 November 2024

Additionally, several key questions remain unaddressed in applying ML to gain insights of ZIF-8 synthesis, although they have the potential to reduce the reliance on time-consuming and costly experiments. These challenges include selecting the most appropriate ML model for specific predictive objectives and developing robust models that offer explainable insights. Among these, the choice of ML model is crucial, since it directly affects prediction accuracy and reliability. Thus, assessing and selecting the appropriate ML model is essential for effectively guiding synthesis. Moreover, ML models should offer not only accurate predictions, but also interpretations of how different synthesis conditions affect ZIF-8 morphology. The interpretability is critical for understanding synthesis process and informing future manufacturing strategies. Developing ML models that can translate data into actionable insights will enable more precise control over ZIF-8 synthesis, but this field remains underexplored.

The development of ML models is also hindered by the availability of databases, especially when considering various synthesis conditions that require many data. However, obtaining such datasets is often challenging due to the complexity and cost of experiments, such as ZIF-8 synthesis and characterization. Thus, maximizing information from limited data becomes essential. For example, small datasets obtained from the early stage of experimentation, where specific synthesis conditions are studied, can provide valuable insights to inform future work and enable more targeted experiments. Although building ML from small datasets can expedite research iterations, this area remains relatively overlooked.

To address these challenges, this work investigates how different synthesis conditions, including the amounts of raw materials, solvent properties, and reaction temperature, affect ZIF-8 morphology, with a focus on its size. Using data collected from our experiments, this work has built three different ML models to predict the size of ZIF-8, which include random forest (RF), support vector regressor (SVR), and neural network (NN). Based on these models, this study further conducted thorough comparison to evaluate their accuracy and predictability.

Findings from this work show the potential of ML models, particularly the NN model, not only for predicting ZIF-8 morphology but also for offering interpretative insights into the synthesis process. These models provide a digital platform for navigating the parameter space defined by various synthesis conditions, thus setting a foundation for the controlled synthesis of ZIF-8 with desirable morphology. By enhancing our ability to predict and control ZIF-8 morphology, these models pave the way for developing more efficient and precise synthesis strategies in the future, thus ultimately broadening the applications of this versatile nanomaterial.

2. Experimental details

2.1. Synthesis and characterization of ZIF-8

A one-pot method by combining zinc nitrate hexahydrate ($Zn(NO_3)_2\cdot 6H_2O$) and 2-methylimidazole (Hmim) was used for ZIF-8 synthesis [5]. Specifically, the objective was to study how varying different synthesis conditions individually and collectively affect ZIF-8 morphology, and to collect data for ML model development.

For ZIF-8 synthesis, the molar ratio of $Zn(NO_3)_2\cdot 6H_2O$ to Hmim was first varied by adjusting the amount of Hmim used, while maintaining the total amount of solvent constant. For example, previous studies, such as those by Kida et al. [6]., have shown that increasing the molar ratio of Zn to Hmim may decrease the average size of the ZIF-8. Based on these findings, three molar ratios of 1:60:2228, 1:100:2228, and 1:140:2228 (Zn:Hmim:solvent) were used in this work.

Additionally, this work investigated the effects of solvent composition on ZIF-8 morphology. Mixtures made of double distilled water (ddH_2O) and methanol were used for adjusting solvent properties, including density, polarity, and viscosity, and for evaluating their effects on ZIF-8 morphology. For example, previous research has shown that the volume ratios between ddH_2O and methanol affects the morphology of ZIF-8, with higher methanol volumes resulting in larger nanoparticles [7,8]. Thus, the volume ratios between methanol and ddH_2O were chosen as 50/50, 70/30, and 90/10 in our experiments.

This study also adjusted the temperature to evaluate its effect on the morphology of ZIF-8 due to conflicting reports. For example, as suggested in the literature, higher temperature accelerates nucleation, which generally reduce the size of ZIF-8 [9], while others have shown limited temperature influence on morphology [10]. Given these, ZIF-8 was synthesized at three different temperatures of 0°C, 24°C, and 50°C to investigate their effects on morphology. These synthesis factors (i.e., molar ratio, solvent composition, and temperature), each with three level, led to 27 unique experimental combinations. To obtain reliable results, replicates of experiments for each combination were performed to collect sufficient data for model development.

After synthesis, ZIF-8 samples were characterized by focusing on the size since it is crucial for applications such as drug delivery, for which the size of ZIF-8 affects endocytosis and drug loading rate[11]. Transmission electron microscopy (TEM) was used to obtain high-resolution images, and the sizes of ZIF-8 were quantified using ImageJ software. Based on the imaging data, 100 nanoparticles of ZIF-8 were identified and analyzed per experiment to determine the size distribution and estimate the average size. The average size data (model output) was further used together with the synthesis factors (model inputs) to develop and validate ML models.

To validate the synthesis and further characterize the ZIF-8, X-ray diffraction (XRD) and Brunauer-Emmett-Teller (BET) analyses were also performed. XRD was used to confirm the crystalline structure and phase purity of the synthesized ZIF-8, while BET analysis was used to obtain information on the specific surface area and pore volume, which offered additional insights into ZIF-8's morphological features and confirmed the success of our experiments.

2.2. Machine learning model development

To address key challenges in optimizing ZIF-8 synthesis and improving predictability of computational tools, this work built and compared three ML models by considering difference in algorithms and our modeling objectives. Random Forest (RF), which is a type of decision tree-based algorithms, is chosen for its capability to ensemble the results from individual decision trees for reducing the effect of data uncertainty. This ability of RF is important since the goal in this study is to build models with small datasets, which may contain uncertainty and affect the modeling results. Thus, an RF model may potentially address such issues and offer insights of the effects of synthesis conditions on ZIF-8 morphology [12]. For the second model, this study focused on the regression-based algorithms and used Support Vector Regressor (SVR). This method was used for its high flexibility in modelling non-linear relationships without requiring explicit mathematical expressions [13]. To leverage the superior self-learning capabilities of neural network (NN) [14], an NN model was built to compare prediction accuracy and model interpretability. By comparing these models, the specific objective in this work was to identify the most effective modeling approach for predicting ZIF-8 morphology and for gaining interpretable insights into the synthesis process of ZIF-8.

An overview of the modeling approach in this work is briefly given in Fig. 1. To build individual ML models, our collected data was divided into training and testing sets. Initially, the training set was used to identify the optimal hyperparameters for each of the three models considered. For this purpose, hyperparameters were randomly assigned to build surrogate models within the searching domains of hyperparameters, which were defined offline for different algorithms. Following this, a grid search method [15] was used to identify the optimal hyperparameters for individual models. To expedite model development and reduce complexity, constraints were also used for these hyperparameters of individual models considered in this study.

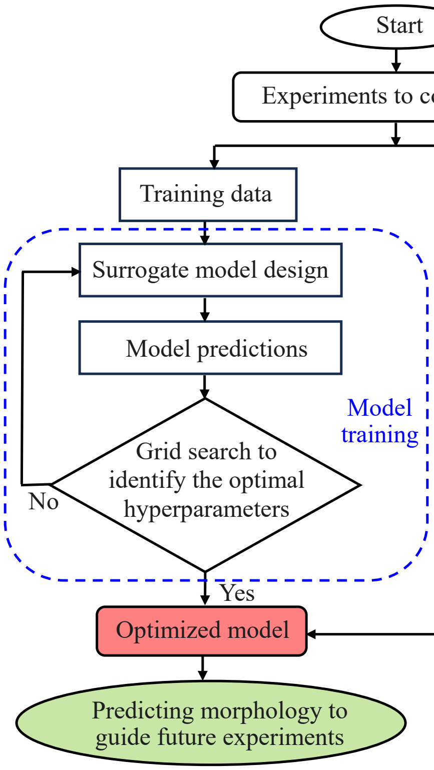

Fig. 1. Schematic overview of the model development and evaluation procedures.

Once the optimal hyperparameters have been identified, they were fixed for the final model calibration. These models describe the relationships between the size of ZIF-8 (the model output) and the synthesis conditions (the model inputs). In this study, these inputs include the amount of Hmim, reaction temperature, and the density, polarity, and viscosity of the solvents used in material synthesis. To evaluate the accuracy and performance of each model, metrics such as R-squared (R^2) and mean squared errors (MSE) were used, which were calculated using equations as follows:

$$MSE = \frac{1}{n}\sum_{i=1}^{n}(y_i - \overline{y}_i)$$

$$R^2 = 1 - \frac{\sum_{i=1}^{n}(y_i - \overline{y}_i)}{\sum_{i=1}^{n}(y_i - \overline{y})}$$

where y_i is the ZIF-8 size determined with collected data, $\overline{y}_i$ represents model predictions, $\overline{y}$ is the mean of ZIF-8 size, and n is the total number of datapoints for MSE and R^2 calculations.

To evaluate model predictability, the testing set that was not used for hyperparameter optimization or model training were used to calculate R^2 and MSE. To provide a comprehensive comparison among models, violin plots were adopted to visualize the distributions of R^2 and MSE, which enabled a visual comparison of central tendencies and variabilities among different models. To achieve this, the collected data was reshuffled to create new, distinct datasets that were not used in the original model training and testing phases. The violin plot analysis and visualization ensured a robust comparison and helped with the identification of the most suitable model for predictive analysis.

3. Results and discussion

3.1. Morphological changes in synthesized ZIF-8

The morphology of ZIF-8 is significantly affected by different synthesis factors, including the amount of Hmim, solvent density, polarity, viscosity, and reaction temperature. Fig. 2 shows some of our representative results of ZIF-8 synthesized under three different conditions. For Fig. 2(a)~(c), ZIF-8 was synthesized at a molar ratio of Zn$(NO_3)_2{\cdot}6H_2O$ to Hmim to solvent of 1:60:2228 at a temperature of 50 °C, using a solvent made from 8 ML of double distilled water (ddH_2O) and 8 ML of methanol. By contrast, Fig. 2(d)~(f) show the results at a lower temperature of 0 °C, while keeping other synthesis factors unchanged. In addition, Fig. 2. (g)~(i) show the results of ZIF-8 made at a different molar ratio of $Zn(NO_3)_2{\cdot}6H_2O$ to Hmim to solvent of 1:140:2228 and at a temperature of 24 °C, using a mixed solvent with 8 ML of ddH_2O and 8 ML of methanol.

As shown in Fig. 2(a) and (d), reducing the synthesis temperature leads to an increase in the size of ZIF-8, by examining several randomly selected ZIF-8 nanoparticles. This trend is further confirmed by the size distributions as given in Fig. 2(c) and (f), for which 100 nanoparticles were identified from TEM images and used for analysis. Furthermore, the size of ZIF-8 increases when both the molar ratio and temperature are adjusted as shown in Fig. 2(g) and (h). Additionally, despite the size changes among different conditions, ZIF-8 nanoparticles maintained their characteristic rhombic dodecahedron shapes with distinct angles and truncated corners for both synthesis conditions as shown in Fig. 2 (b), (e), and (h). These results are consistent with existing literature on ZIF-8 morphology [6]. It is important to note that the size of ZIF-8 at 24 °C is different from these at 0 °C and 50 °C, due to changes in both the molar ratio and temperatures. At 24 °C, as shown in Fig. 2(g), the increased concentration of Hmim likely promoted ZIF-8 nucleation and growth, thus resulting in larger crystals. However, when the molar ratio was kept constant, as in the experiments shown in Fig. 2(a) and (d), the size of ZIF-8 at 24 °C changed from 59 nm to 67 nm, which is similar to the sizes observed at 0 °C and 50 °C. This further suggests that the changes in both molar ratio and temperature are the primary factors that can affect ZIF-8 morphology.

All ZIF-8 samples were characterized using XRD. Fig. 3(a), (b), and (c) show the XRD spectra for ZIF-8 synthesized under three conditions described earlier. Fig. 3(a) shows the XRD results for samples prepared with a molar ratio of 1:140:2228 at 24 °C, using 8 ML of ddH_2O and 8 ML of methanol as the solvent. Fig. 3(b) shows the results at a molar ratio of 1:60:2228 at 0°C, whereas Fig. 3(c) shows the results at 50°C under the same molar ratio. These XRD patterns indicate that the synthesized ZIF-8 samples are highly crystalline, thus suggesting that variations in the experimental conditions did not significantly affect the crystal structures.

Additionally, BET analysis was performed under N_2 at 77.35 K to characterize the surface area and micropore volume of the synthesized ZIF-8 samples. For the three aforementioned experimental conditions, the surface area of ZIF-8 synthesized at 50 °C with a molar ratio of 1:60:2228 was approximately 1410.1 m^2/g, with a micropore volume of about 0.7036 cm^3/g. In contrast, ZIF-8 synthesized at 0 °C with the same molar ratio exhibited a surface area of about 1260.83 m^2/g and a micropore volume around 0.877 cm^3/g. ZIF-8 synthesized with a molar ratio of 1:140:2228 at 24 °C has a surface area around 1140.94 m^2/g and a micropore volume approximately 0.863 cm^3/g. These material characterization results in this study are consistent with reported values in the literature [16].

3.2. ML model development and comparison

Selecting the most suitable ML modelling approach and optimizing model hyperparameters for predictive analysis are critical. The grid search was used to identify the optimal combinations of

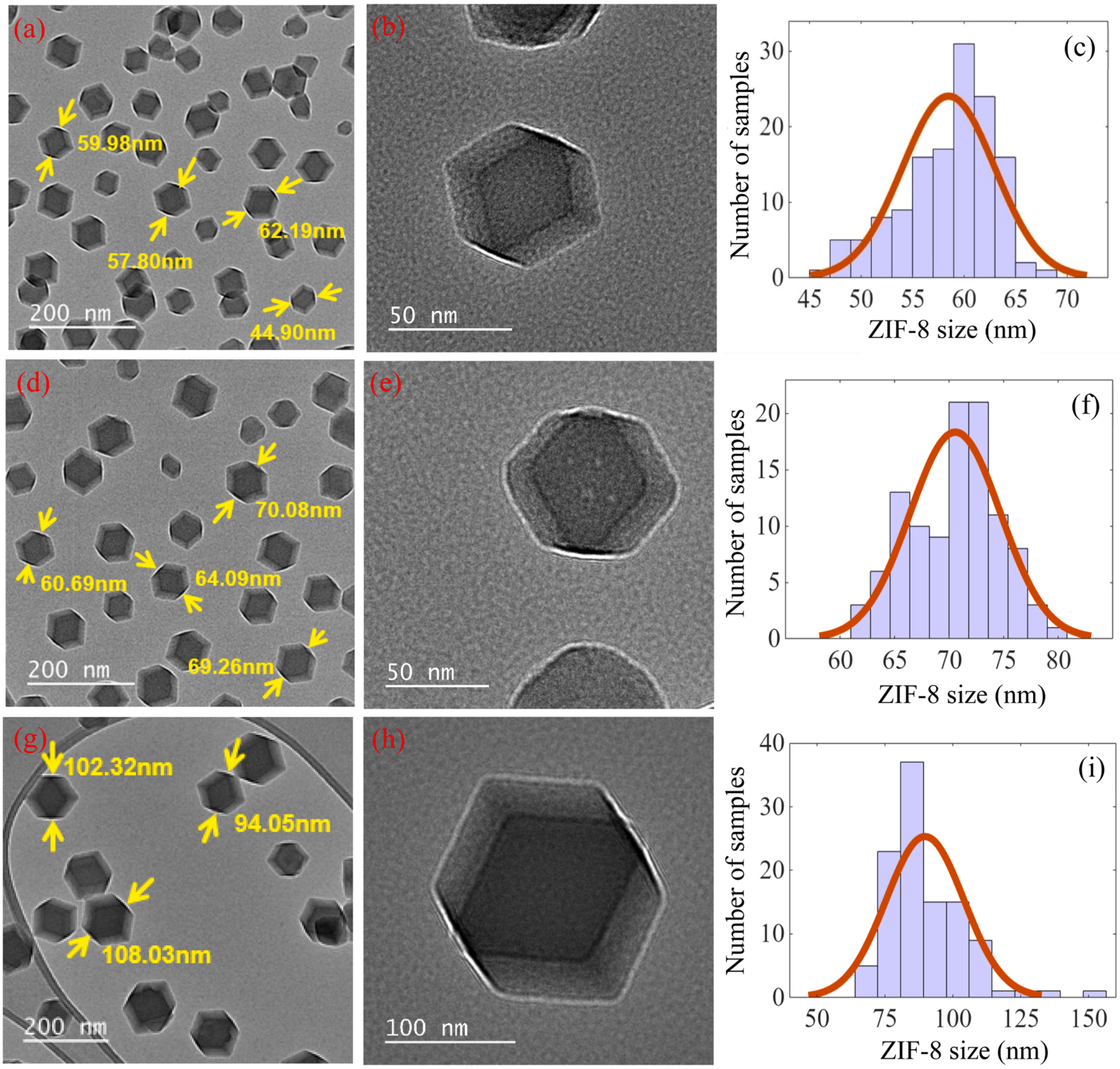

Fig. 2. Characterization results of ZIF-8 morphology: (a), (b), (d), (e), (g) and (h) present the size and structure of ZIF-8 synthesized under three different conditions, (c), (f), and (i) show the size distributions of the materials based on 100 characterized samples of ZIF-8.

hyperparameters for individual models. Fig. 4 shows the heatmaps generated from the grid search for different models, where R^2 was used to evaluate the effect of various combinations of two specific hyperparameter on model training. In each heatmap, the rows and columns represent different values of selected hyperparameters. Each cell shows the R^2 value corresponding to a specific combination of these hyperparameters defined by its row and column. Color changes within the heatmaps also visually demonstrate the effect of these combinations on model performance, thus facilitating the optimization of hyperparameters.

To build the RF model, this work focused on optimizing several hyperparameters to improve its performance. Simulations were performed to study if bootstrapping that adjusts random sampling with replacements could improve model accuracy. Additionally, this work optimized the minimum samples required for leaf nodes in order to build a smooth RF model, tested the minimum samples required for splitting nodes to avoid overfitting, and adjusted the maximum depth of trees to improve model generalization. Furthermore, the number of decision trees were optimized to balance the tradeoff between computational cost and model accuracy. Given these hyperparameters create a multidimensional space that is challenging to visualize, Fig. 4(a) shows a heatmap of R^2 for the combination of the number of trees and the minimum samples for leaf as an example. As seen, increasing the number of trees improves the performance of the RF model.

For SVR model, this work optimized the regularization factor (C) to find a tradeoff between model accuracy and complexity while avoiding overfitting. Both Gaussian and Sigmoid kernels were considered initially to determine which kernel better captures patterns in the data. Additionally, the effect of gamma and epsilon were studied, since these two parameters define the acceptable margin of prediction errors and affect the model's robustness [17]. Similar to the RF model, Fig. 4(b) shows a heatmap of R^2 values for the combinations between the regulation parameter and epsilon of the SVR model. This heatmap suggests that higher values of these hyperparameters lead to increased model accuracy.

For the NN model, this work focused on identifying the optimal numbers of hidden layers and neurons per layer, considering our data size. Similar to the other two models, this creates a multidimensional parameter space for the heatmap based visualization. Thus, Fig. 4(c) only shows how different combinations of the total number of hidden layers and the number of neurons used in the first hidden layer affect the model performance for demonstration. The cell values and color gradients in Fig. 4(c) indicate complex relationship between these two hyperparameters since no clear trends can be observed. Using the grid

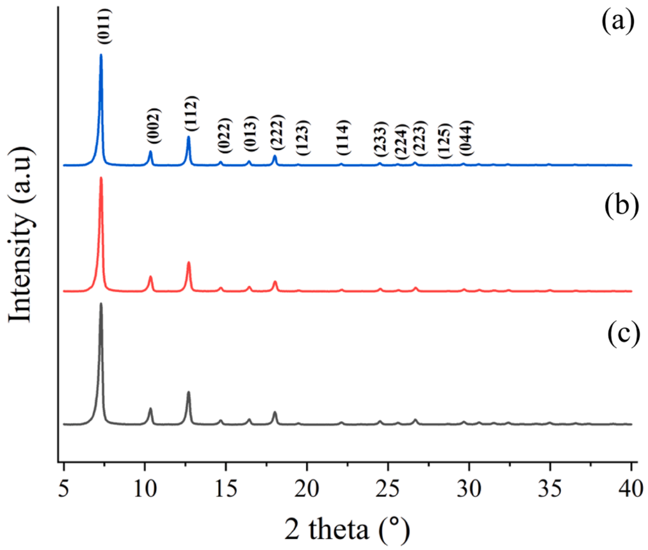

Fig. 3. XRD characterization to confirm the crystal structures of ZIF-8 synthesized under different conditions.

search algorithm, Table 1 summarizes the optimal hyperparameters of each model.

To evaluate and compare the accuracy and predictability of different models, the MSE and R^2 values were calculated between the predicted sizes and these estimated from imaging data. For visualization and demonstration, scatter plots were used for one set of training and testing data as shown in Fig. 5. In these plots, red triangles represent the training data, while blue circles represent testing data points. In all models for both the training and testing datasets, the predictions are randomly scattered around the perfect prediction line (the dotted red line), thus suggesting that these ML models can provide accurate predictions.

Additionally, to better demonstrate the capability of each model for dealing with potential uncertainty in the data, the collected data was shuffled to create multiple distinct training and testing datasets. Following this, multiple rounds of model evaluation were performed using these datasets and calculated the MSE and R^2 values in each round. To ensure the reliability of analysis, violin plots were used to visualize the distributions of MSE and R^2 for both the training and testing phases. The comparison results are shown in Fig. 6, where the red markers represent the median values of MSE and R^2 in these violin plots for each model.

As shown in Fig. 6(a) and (c), different models have demonstrated distinct performance during the training phase. The SVR model has significantly poor performance as compared to other models. Its larger MSE and smaller R^2 values, with a wider and spread distributions of these metrics, indicate the less robustness and lower generalization capability of the SVR model. In contrast, the RF and NN models have smaller MSE and larger R^2 values, which suggests that these models have the capability to capture and describe the variability in the training data. Additionally, the R^2 values for the RF and NN models are above 0.9, thus confirming their strong predictability on training data.

To further compare the performance of these models, Fig. 6(b) and (d) show the violin plots of the MSE and R^2 during the testing phases, using the models from the training phases. As compared to the results from the training phases, the NN model outperforms the other models.

Table 1
Hyperparameters of the RF, SVR, and NN models.

Models	*Optimized hyperparameters*
RF	Bootstrapping was set to False. The minimum samples of leaf and the minimum samples of split were optimized as 1 and 3, respectively. The total number of trees was set to 10 and the maximum depth of trees was set to 20.
SVR	Gaussian kernel function was used. The regularization factor, gamma, and epsilon values were set to 30, 1, and 5, respectively.
NN	The optimal number of hidden layers was 3 and the number of neurons used in each layer was 30, 18, and 6, respectively.

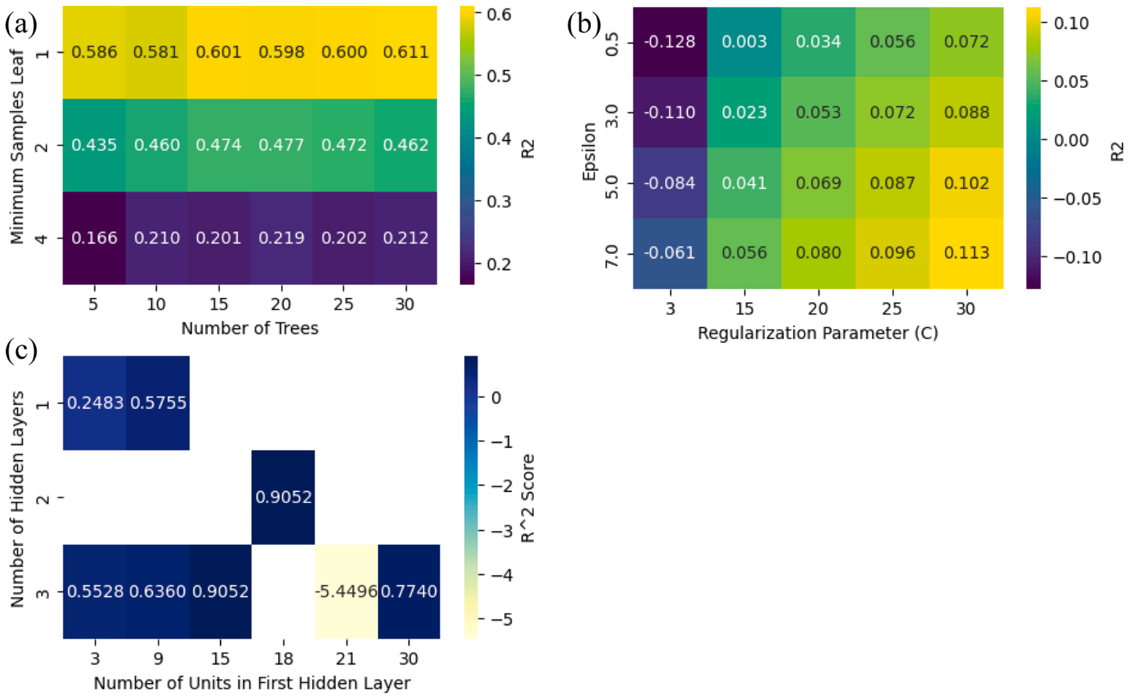

Fig. 4. Heatmaps illustrating the effect of hyperparameter combinations on R^2 values: (a) shows how variations in the number of trees and minimum samples per leaf affect R^2 for the RF model, (b) shows the effects of regularization parameter and epsilon on R^2 for the SVR model, and (c) demonstrates how the total numbers of hidden layers and neurons in the first hidden layer jointly affect R^2 for NN model.

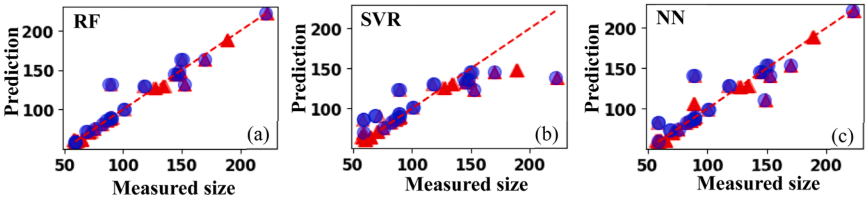

Fig. 5. Predicted *vs.* actual mean values of ZIF-8 size (nm): (a), (b), and (c) show the predictions for the RF, SVR, and NN models, respectively. Red triangles represent the training data, while blue circles represent testing data. The x-axis shows the estimated ZIF-8 size from TEM images using ImageJ and the y-axis show the predicted size using these models and measurements of synthesis conditions.

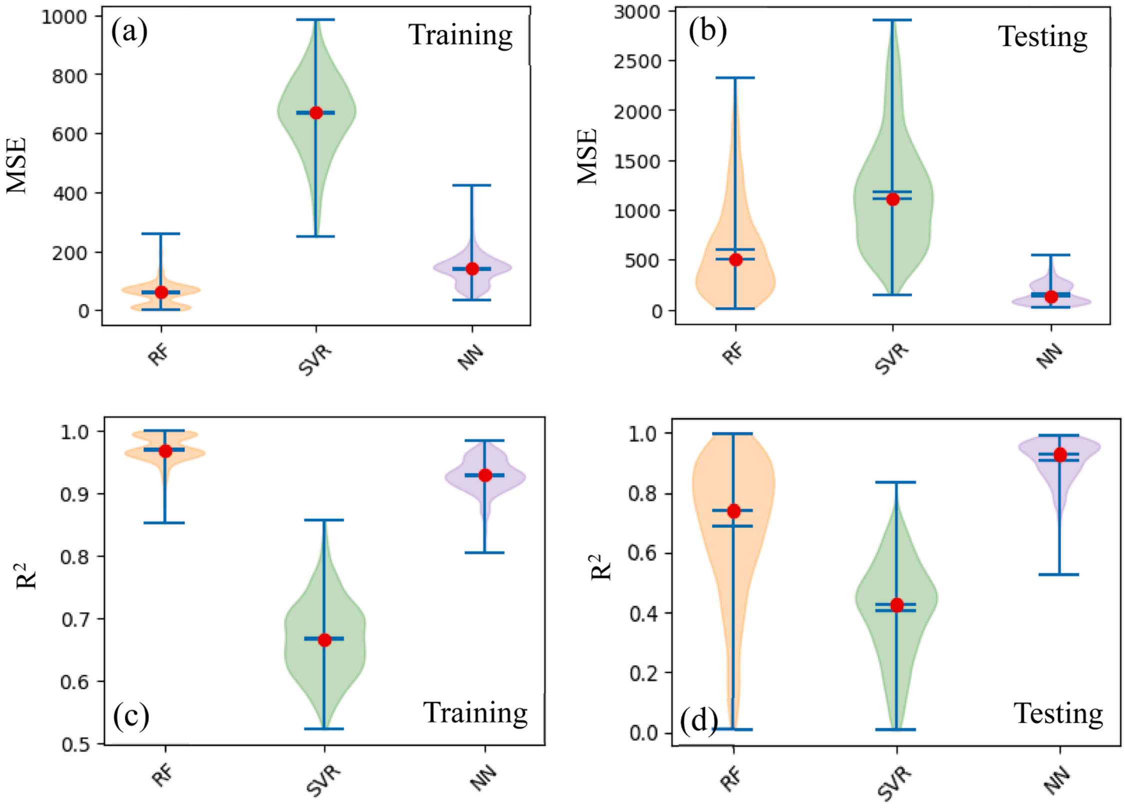

Fig. 6. Violin plots evaluating model consistency and generality: (a) and (b) show the MSE values for the training and testing datasets of the RF, SVR, and NN models respectively; (c) and (d) present the R^2 values for the training and testing datasets using the same models.

The NN model exhibits much smaller MSE and larger R^2 values, each with a narrower and more concentrated distribution. This indicates that the NN model is more consistent and accurate when dealing with different datasets unseen during the training phases. In comparison, other models all have wider distributions of the MSE and R^2 metrics, which indicates their less effective generalization to unseen data that might be distinct from training data. Integrating these observations from Fig. 6, the NN model's narrower distributions of MSE and R^2 across both the training and testing phases confirm its superior performance for morphology prediction.

The superior performance of the NN model may come from three aspects. (i) The NN's model structures may help improve prediction performance. In this work, the NN's model structure is optimized by adjusting the number of hidden layers and the number of neurons in individual layers. This optimization allows the NN model to effectively extract information from data and handle the complex nonlinear relationships between the morphology of ZIF-8 and synthesis conditions, thus contributing to the model's robustness and generalization performance. (ii) The NN model may benefit from a more focused hyperparameters optimization. By concentrating on a limited set of hyperparameters in this work, namely, the hidden layer and neurons, the risk of overfitting can be reduced as compared to other models that required extensive hyperparameter tuning to obtain similar performance as the NN model. For example, the RF model has to use the grid search method to adjust multiple parameters to obtain similar MSE results as the NN model, which include the number of decision trees, maximum tree depth, minimum samples per node for splitting, minimum samples per leaf, and bootstrapping. This complexity may lead to overfitting, thus causing the variability in the MSE and R^2 distribution during the testing phases with unseen datasets. (iii) The algorithm itself used for developing each individual model may play a significant role in performance. While the RF model performs well on training datasets, it struggles with the testing datasets, which is possibly caused by the potential imbalances and representative issues in datasets. Essentially, RF model uses bagging with random subsets of training data to build multiple decision trees, which may limit its capability to interpret unseen data from other subsets. Based on the results in Fig. 6, the NN model has better overall performance with larger R^2 and smaller MSE values, as compared to decision tree and regression-based modeling approaches.

3.3. Explainable analysis using ML models

Computational models offer valuable insights into how different synthesis conditions affect the morphology of ZIF-8. This work focuses on RF, SVR, and NN models due to their distinct methodological strengths. For example, as an ensemble method, RF integrates results from multiple decision trees to make model prediction, which addresses data uncertainty and improves model robustness and stability. The SVR model is chosen for its ability to handle complex and nonlinear relationships since liner models may not sufficiently describe the effects of synthesis conditions on ZIF-8 morphology. Moreover, the NN model is selected for analysis due to its superior flexibility in modeling complicated patterns and relationships in data. Using these models, the objective in this work is to identify the most significant conditions that affect the size of ZIF-8 for future further studies aimed to address limitations in current synthesis approaches that often focus on experimentally adjusting one condition at a time. Ranking significant synthesis conditions will also set the basis to prioritize future experiments by focusing on these most critical factors to accelerate knowledge discovery and ZIF-8 synthesis with tunable morphology.

To achieve this, SHapley Additive exPlanation (SHAP) analysis were used to rank the effect of synthesis conditions on ZIF-8 size and validate these findings with the permutation analysis. Fig. 7 shows the SHAP summary plots and bar plots of the permutation analysis, which quantitatively and visually demonstrate the impacts of synthesis conditions. The results in Fig. 7 indicate that the amount of Hmim in reactions, solvent properties, and temperature can affect ZIF-8 synthesis, but with varying degrees of impacts. For example, the SHAP summary plots in Fig. 7(a), (c), and (e) show that Hmim and polarity are consistently identified as the most significant conditions across the RF, SVR, and NN

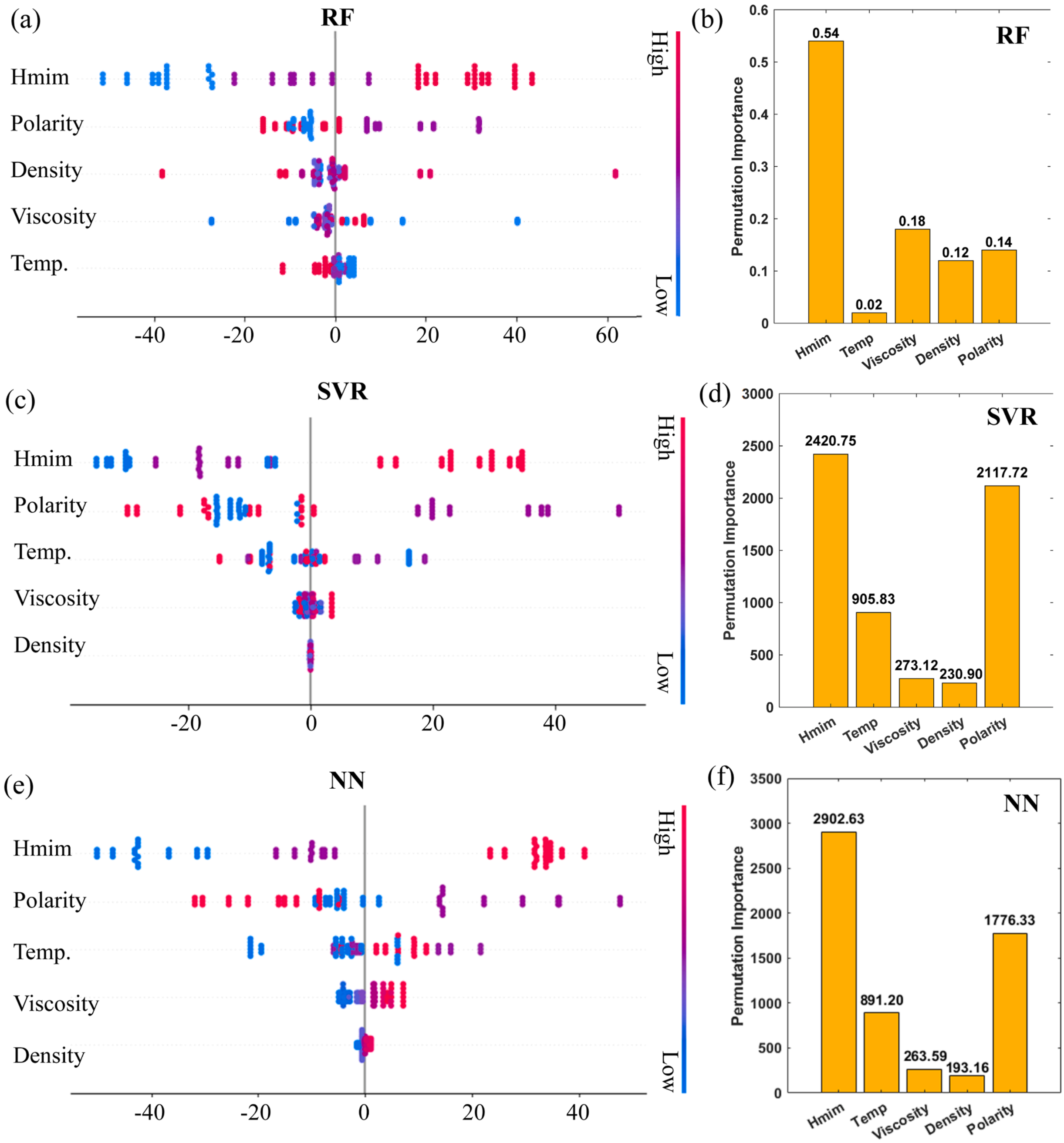

Fig. 7. Visual demonstration and comparison of the effect of synthesis conditions on ZIF-8: (a), (c), and (e) show the SHAP analysis for the RF, SVR, and NN models, respectively, while (b), (d), and (f) present the results of permutation analysis using the same models.

models. Additionally, the SHAP plots of Hmim exhibit spare dot distributions with different colors that highlight the contribution of each datapoint for analysis, which confirms the significant effect of Hmim on ZIF-8 synthesis. In contrast, density as shown in these figures, particularly Fig. 7(c) and (e), has more centralized dot distributions, which suggests that density has less influence and might cause model redundancy for the SVR and NN models.

Additionally, there are discrepancies in the rankings across different models. While the SVR and NN models provide consistent rankings, the RF model has different results. For example, all three solvent properties have a greater impact on ZIF-8 size in the RF model as shown in Fig. 7(a), as compared to reaction temperature. This discrepancy may arise from several factors, which include how data from synthesis experiments are used for RF model development and the methodological difference in modeling methods. Both SVR and NN models can more effectively capture the nonlinear relationships between synthesis conditions and the size of ZIF-8 by looking into data directly [18]. In contrast, the RF model as an ensemble decision tree-based method may prioritize synthesis conditions differently based on how the algorithm splits the data for training individual trees, which affects the final ranking of conditions when merging the results from individual trees.

Moreover, the RF model quantifies the effect of synthesis conditions on ZIF-8's size by measuring changes in the training objective function across trees, thus potentially contributing to different rankings compared to the SVR and NN models. The discrepancy in SHAP value rankings between the RF model and the SVR and NN models can be also introduced by how these modeling algorithms treat discrete datapoints. Although synthesis conditions can be theoretically continuous, conducting massive experiments is impractical and only limited numbers of experiments were conducted to collect discreate data points for model training. As compared to the SVR and NN models that can generalize well from sampled discrete data, RF model is more sensitive due to its decision tree-based structure, which splits data based on specific values. This could further introduce sparse and concentrated datapoints that may shift the ensemble results towards these dense regions of data, thus leading to biased results. This methodological difference may affect feature importance calculation and contribute to ranking discrepancies.

As shown in Fig. 7(b), (d), and (f), permutation analysis is also used to validate and compare SHAP values for individual modeling methods. For the SVR and NN models, permutation analysis confirms that Hmim and polarity are the most significant synthesis conditions, followed by reaction temperature, viscosity and density. However, the RF model provides different rankings among solvent properties. Specifically, the RF model ranks Hmim as the most significant condition, but identifies viscosity as the second most significant factor, according to permutation analysis, where the SHAP summary plot of the same model shows polarity as the second most important. This discrepancy may be caused by the fact that SHAP accounts for the interactions among synthesis conditions, while permutation analysis emphasizes the impact of individual conditions.

Recognizing the changes in rankings among three solvent properties for the RF model, it is important to point out that viscosity, density, and polarity show similar permutation values in Fig. 7(b). The similarity in permutation values indicates their comparable effects on ZIF-8 synthesis, though Hmim remains the impactful factor. For example, the permutation analysis shows values of 0.14 for polarity, 0.18 for viscosity, and 0.12 for density. These values are significantly lower than the value of 0.54 for Hmim. This suggests that while all solvent properties have similar effects, Hmim can directly control ZIF-8 nucleation and growth, which may lead to significant size changes in ZIF-8 with even minor variations in the amount of Hmim.

The consistent ranking about the effect of synthesis conditions on ZIF-8 from the SHAP summary plots and permutation analysis for both the SVR and NN models confirms their robustness in identifying influential synthesis conditions. The agreement between the SVR and NN models also cross validates their accuracy and suggests a reliable understanding of how synthesis conditions affect the morphology of ZIF-8. In contrast, the different rankings from the RF model, particularly among solvent properties, highlight the complex interactions and varying impacts of these conditions. For example, viscosity affects mass transfer during synthesis, which changes molecules movements and bonding between zinc ions and organic ligands. On the other hand, polarity is related to dielectric constants and dipole moments, which affects molecular interactions in the reactions. Although mass transfer affects how molecules interact, viscosity does not directly affect polarity. These may highlight the inherent complex nature among different solvent properties in the synthesis process.

In summary, integrating SHAP and permutation analyses with ML models provides a thorough understanding of individual and interactive effects of synthesis conditions. This combined approach improves model explainability and provides implementable insights for experimental design. Leveraging the combined analytical methods, it may become possible to narrow down the number of conditions to test for material synthesis optimization. The reliability of SVR and NN for synthesis condition analysis, coupled with the unique insights from RF, also highlights the value of using multiple models for a comprehensive evaluation. Considering the accuracy and consistency of the NN model compared to other models, we therefore focus on using the NN model for predictable analysis below.

3.4. Predictable analysis using ML models

To illustrate the potential applications of the NN model, how changes in synthesis conditions affect ZIF-8 size were visualized. However, visualizing predictions using the NN model has its inherent challenges due to the five-dimensional nature of the synthesis conditions (or five model inputs). To address this, two-dimensional (2D) slices were used to demonstrate the relationship between the size of ZIF-8 and a pair of synthesis conditions as shown in Fig. 8. Specifically, this work focuses on visualizing the joint effect of Hmim with other conditions since Hmim is the dominating condition that affects ZIF-8 size based on the SHAP and permutation analyses above.

Using the NN model, Fig. 8(a) shows the predicted joint effects of Hmim and polarity on the size of ZIF-8, with other synthesis conditions held constant at their mean values. The color bar indicates the size of ZIF-8, and these white dotted lines represent contours that distinguish regions with different sizes. As seen, the size of ZIF-8 increases when polarity is lower and the concentration of Hmim is higher. This is likely because a lower polarity increases the solubility of Hmim, thus increasing the concentrations of the ligand in the solution. The higher concentration of Hmim therefore can accelerate nucleation and promote the growth of larger ZIF-8 by providing more ligands. In contrast, a decrease in the concentration of Hmim results in a limited number of ligands in the solution, thus leading to formation of smaller ZIF-8.

Additionally, the contours in Fig. 8(a) are curvy and nonuniformly distributed within the 2D parameter space defined by Hmim and polarity. This indicates a nonlinear relationship between these two synthesis conditions, which may present challenges for controlling the ZIF-8 synthesis process, thus requiring additional attention in future large-scale manufacturing of ZIF-8. For example, at low Hmim concentrations, even small changes in polarity can cause significant variations in the size of ZIF-8, as illustrated by the narrow gap between adjacent contours in Fig. 8(a). Understanding this nonlinear relationship is critical for precise control over ZIF-8 size. By analyzing and visualizing how different concentrations of Hmim interact with varying polarities, it becomes possible to tailor the synthesis conditions to achieve desired morphology. For example, when larger ZIF-8 is preferable, optimizing both the solvent polarity and Hmim concentration within the identified regions can help achieve the desired results. Similarly, if smaller ZIF-8 is required, adjusting these parameters can help refine the synthesis process.

A similar nonlinear relationship can be also observed between Hmim

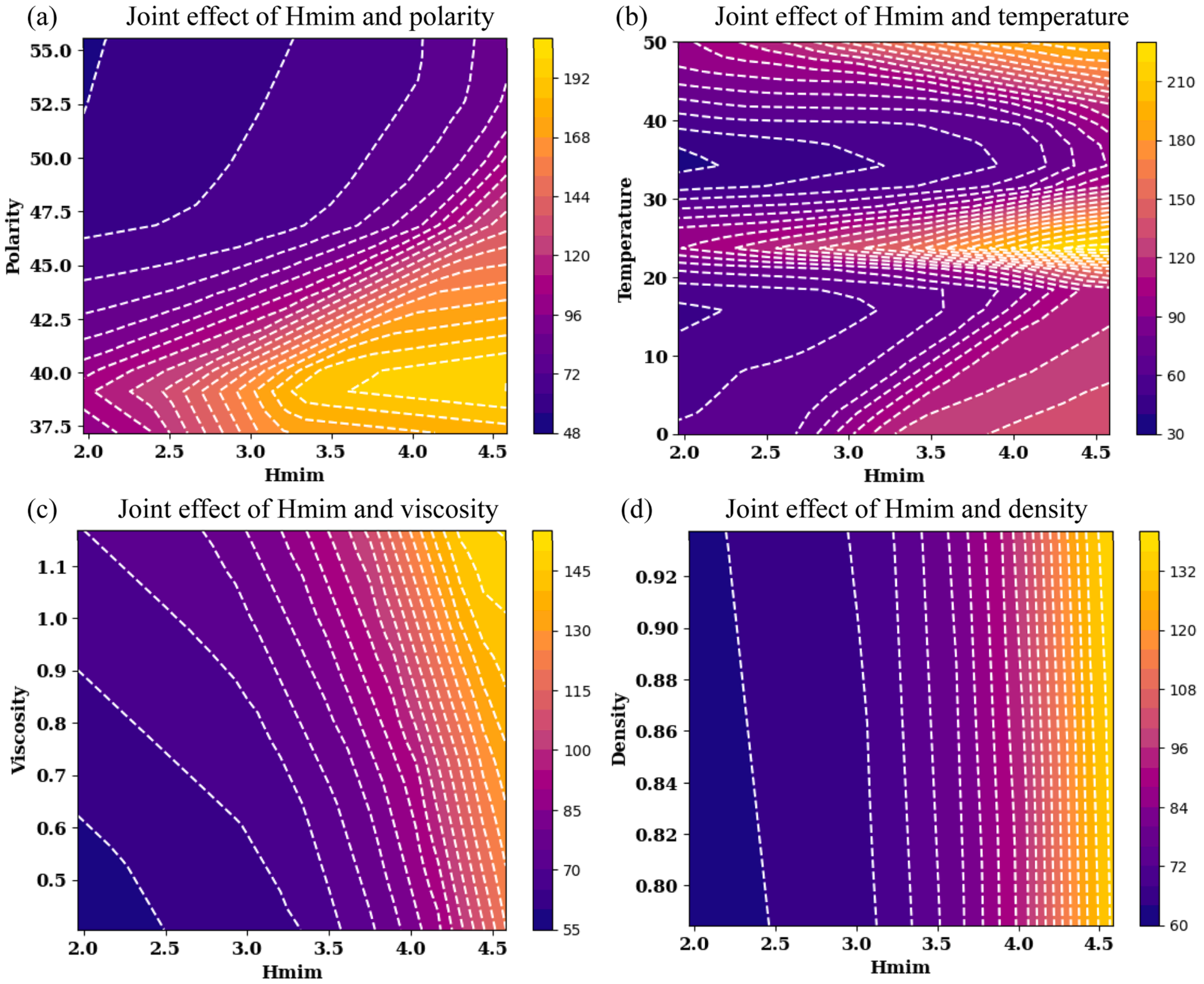

Fig. 8. Predictive analysis of the effect of synthesis conditions on ZIF-8 size: (a) predicts the joint effect of varying polarity and Hmim on ZIF-8, (b) shows the combined effect of temperature and Hmim on ZIF-8, (c) demonstrates how viscosity and Hmim collectively affect ZIF-8, and (d) shows the effect of density and Hmim on ZIF-8.

and temperature as shown in Fig. 8(b). As seen, temperature plays a key role in ZIF-8 synthesis and must be carefully selected. For temperature below 20°C, the size of ZIF-8 increases with higher Hmim concentrations. Likely, this is because, at low temperatures, low concentrations of Hmim, cannot provide sufficient ligands to facilitate ZIF-8 growth, thus leading to the formation of small particles. In contrast, with the temperature in the range between 20 °C and 30 °C, the size of ZIF-8 is larger and increases with higher Hmim concentrations. This observation suggests that this temperature range may provide sufficient kinetic energy to improve reactant diffusion, thus creating more opportunities for molecular interactions and ZIF-8 growth. In this case, this temperature range can likely be the desired synthesis condition when larger ZIF-8 is preferred for specific applications.

When the temperature is higher than 30 °C, these contours that describe the changes in ZIF-8 size appear to follow the patterns similar to these observed at temperature below 20 °C. The possible reason is that a high temperature increases molecular kinetic energy to accelerate reaction, but also reduces interaction time, as the speed of molecules in the solution increases. The reduced reaction time and rapid movement of Hmim at a high temperature thus limits ZIF-8 growth. However, increasing the concentration of Hmim at high temperature can provide more ligands, which results in larger ZIF-8.

It is also important to note that during our simulations with the NN model, other factors related to the solvent properties were fixed by using their mean values. This has resulted in different synthesis conditions in our experiments that focused on only a few synthesis conditions since the goal was to build models with a limited dataset to demonstrate the predictivity of ML models. From these simulated changes using the NN model, it can be inferred that maintaining an optimal reaction temperature is vital for balancing ZIF-8 growth rates and obtaining the desired ZIF-8 morphology.

Additionally, unlike the relationship between Hmim and polarity in Fig. 8(a), the relationship between Hmim and temperature appears to have multiple directional trends. This may be due to the limitations of the experimental design as this work mainly focused on three temperatures with a relatively large gap between the median and highest temperatures. This suggests a critical need for further extensive experimental validation, which is planned for future. However, considering the predictability of the NN model, it now becomes possible to visualize and study the changes in ZIF-8 size, while adjusting multiple synthesis conditions simultaneously.

A nonlinear relationship between viscosity and the concentration of Hmim is also observed in Fig. 8(c). High viscosity can slow the diffusion of reactants, but the high concentration of Hmim can still promote faster ZIF-8 growth. Thus, the top right corner of Fig. 8(c) shows that this combination can lead to a larger ZIF-8. In contrast, low viscosity facilitates diffusion, but low Hmim concentration results in limited ligand availability. This typically leads to slower growth and smaller ZIF-8, as shown in the bottom left corner of Fig. 8(c).

Compared to the relationship between Hmim and temperature or viscosity, the relationship between Hmim and density appears to be linear as shown in Fig. 8(d). The size of ZIF-8 increases as the concentration of Hmim increases as expected. This is because density affects the overall mass and volume of the solution, but it doesn't directly determine the molecular interactions or diffusion rates in the same way as viscosity and polarity. Although density changes can indirectly affect reaction conditions, such as by affecting how reactants are mixed, its role in reaction is less significant, as compared to the direct effects of viscosity and polarity. This aligns well with the SHAP summary plots and permutation analysis, as the SHAP values of density are close to zero for both the SVR and NN models as shown in Fig. 7(c) and (e), thus confirming that density is not crucial for the models' predictions.

3.5. *Prospect of ML assisted analysis*

This work demonstrates that integrating ML models with ZIF-8 synthesis can provide computational tools to improve the efficiency and address the limitations of conventional trial-and-error approaches. This study focused on several synthesis conditions, which generated training data to computationally evaluate the collective effects of these conditions on ZIF-8 size. The combination of modeling and experimental data shows the potential of ML to extract meaningful insights from limited datasets, even when the dimension of the synthesis condition space is high due to the complex relationships among different factors. This illustrates how ML can effectively guide experimental design and optimize synthesis conditions, even considering the constraints of small dataset and their correlations.

This work also exemplifies the synergy between ML models and experimental methodologies, which will set the basis for precise control over the morphology of ZIF-8 by adjusting reaction conditions, while facilitating rapid experimentation. It is expected that, in ongoing studies, automating the adjustment of key synthesis conditions, such as the amount of Hmim, can reduce the number of required experiments and further improve efficiency. These analyses and observations here, such as the 2D visualizations of synthesis conditions, highlight the capability of the ML-based approaches to uncover complex interactions that may be undetectable via conventional techniques. Despite technical difficulties, like the extensive validation of results from ML models, the integration of ML with advanced experimental setups holds promise for revolutionizing ZIF-8 synthesis. Such an experimental and computational integrated strategy will build a paradigm for future manufacturing, expedite ZIF-8 synthesis, and accelerate the adoption of this material for various applications.

4. Conclusions

This work experimentally investigated how synthesis conditions affect the morphology of ZIF-8 and built three ML models to predict the effect of these conditions on ZIF-8 size. The predictive accuracy of the RF, SVR, and NN models were compared using MSE and R^2 metrics, which highlight the superior performance of NN model for explainable modeling. The findings from this work build the foundation for future experimental validations to identify critical synthesis conditions and better understand the complex relationship between synthesis conditions and ZIF-8 size. These computational tools to assist ZIF-8 synthesis also offer an efficient strategy for optimizing experimental conditions and advancing manufacturing capabilities.

CRediT authorship contribution statement

Dongping Du: Writing – review & editing, Methodology, Formal analysis, Data curation. **Cristina Sanchez:** Investigation. **Yuncheng Du:** Writing – review & editing, Writing – original draft, Visualization, Validation, Supervision, Software, Resources, Project administration, Methodology, Investigation, Funding acquisition, Formal analysis, Data curation, Conceptualization.

Declaration of Competing Interest

The authors declare that they have no known competing financial interests or personal relationships that could have appeared to influence the work reported in this paper.

Acknowledgements

This work was supported by the National Science Foundation, grant numbers 2143268 and 2426614.

Data Availability

Data will be made available on request.

References

[1] H.D. Lawson, S.P. Walton, C. Chan, Metal–organic frameworks for drug delivery: a design perspective, ACS Appl. Mater. Interfaces 13 (6) (2021) 7004–7020, https://doi.org/10.1021/acsami.1c01089.

[2] X. Liu, Y. Wang, J. Yuan, X. Li, S. Wu, Y. Bao, Z. Feng, F.H.Y. Ou, Prediction of the ibuprofen loading capacity of MOFs by, Mach. Learn. *Bioeng.* 9 (10) (2022) 517, https://doi.org/10.3390/bioengineering9100517.

[3] N. Pouyanfar, M. Ahmadi, S.M. Ayyoubzadeh, F. Ghorbani-Bidkorpeh, Drug delivery system tailoring via metal-organic framework property prediction using machine learning: a disregarded approach, Mater. Today Commun. 38 (2023) 107938, https://doi.org/10.1016/j.mtcomm.2023.107938.

[4] J.A. Allegretto, D. Onna, S.A. Bilmes, O. Azzaroni, M. Rafti, Unified roadmap for ZIF-8 nucleation and growth: machine learning analysis of synthetic variables and their impact on particle size and morphology, Chem. Y. Mater. 36 (2024) 5814–5825, https://doi.org/10.1021/acs.chemmater.4c01069.

[5] X. Guo, M. Zhang, L. Lv, One-pot synthesis of multifunctional metal–organic frameworks for magnetic resonance/optical imaging, Mater. Lett. (2021) 129025, https://doi.org/10.1016/j.matlet.2020.129025.

[6] K. Kida, M. Okita, K. Fujita, S. Tanaka, Y. Miyake, Formation of high crystalline ZIF-8 in an aqueous solution, CrystEngComm 15 (2013) 1794–1801, https://doi.org/10.1039/C2CE26847G.

[7] C. Jin, H. Shang, Synthetic methods, properties and controlling roles of synthetic parameters of zeolite imidazole framework-8: a review, J. Solid State Chem. 297 (2021) 122040, https://doi.org/10.1016/j.jssc.2021.122040.

[8] A. Tezerjani, R. Halladj, S. Askari, Different view of solvent effect on the synthesis methods of zeolitic imidazolate framework-8 to tuning the crystal structure and properties, RSC Adv. 11 (2021) 19914–19923, https://doi.org/10.1039/D1RA02856A.

[9] C. Tsai, E. Langner, The effect of synthesis temperature on the particle size of nano-ZIF-8, Micro M. M. 221 (2016) 8–13, https://doi.org/10.1016/j.micromeso.2015.08.041.

[10] J. Beh, J. Lim, E. Ng, B. Ooi, Synthesis and size control of zeolitic imidazolate framework-8 (ZIF-8): from the perspective of reaction kinetics and thermodynamics of nucleation, Mater. Chem. Phys. 215 (1) (2018) 393–401, https://doi.org/10.1016/j.matchemphys.2018.06.022.

[11] J.J. Rennick, A. Johnston, R.G. Parton, Key principles and methods for studying the endocytosis of biological and nanoparticle therapeutics, Nat. Nanotechnol. 16 (2021) 266–276, https://doi.org/10.1038/s41565-021-00858-8.

[12] P. Xu, X. Ji, M. Li, W. Lu, Small data machine learning in materials science, NPJ Comput. Mater. 9 (2023) 42, https://doi.org/10.1038/s41524-023-01000-z.

[13] M. Sabzekar, S.M.H. Hasheminejad, Robust regression using support vector regressions, Chaos Solitons Fractals 144 (2021) 110738, https://doi.org/10.1016/j.chaos.2021.110738.

[14] X. Zhang, B. Gakkaggerm, S. Liu, B. Kailkhura, A. Hiszpanski, T.Y. Han, Explainable machine learning in materials science, NPJ Comput. Mater. 8 (2022) 204, https://doi.org/10.1038/s41524-022-00884-7.

[15] A.M.R. Wang, S. Kauwe, A. Oliynyk, A. Gurlo, J. Brgoch, K. Persson, T. Sparks, Machine learning for materials scientists: an introductory guide toward best practices, Chem. Mater. 32 (12) (2020) 4954–4965, https://doi.org/10.1021/acs.chemmater.0c01907.

[16] W. Sun, X. Zhai, L. Zhao, Synthesis of ZIF-8 and ZIF-67 nanocrystals with well-controllable size distribution through reverse microemulsions, Chem. Eng. J. 289 (2016) 59–64, https://doi.org/10.1016/j.cej.2015.12.076.

[17] N. Sathiparan, Predicting compressive strength of grouted masonry using machine learning models with feature importance analysis, Mater. Today Commun. 41 (2024) 110487, https://doi.org/10.1016/j.mtcomm.2024.110487.

[18] W. Zhou, Z. Yan, L. Zhang, A comparative study of 11 non-linear regression models highlighting autoencoder, DBN, and SVR, enhanced by SHAP importance analysis in soybean branching prediction, Sci. Rep. 14 (2024) 5905, https://doi.org/10.1038/s41598-024-55243-x.